ChemCatChem

Research Article
doi.org/10.1002/cctc.202400371

Chemistry Europe
European Chemical Societies Publishing

www.chemcatchem.org

Spray-dried Ni-Co Bimetallic Catalysts for Dry Reforming of Methane

Gerrit Küchen[+],[a] Vinzent Olszok[+],[b] Bjarne Kreitz,[c] Christoph Mahr,[d] Andreas Rosenauer,[d] Thomas Turek,[a] Alfred P. Weber,[b] and Gregor D. Wehinger*[e]

Dry reforming of methane (DRM) is an attractive reaction for synthesis gas production, since it converts two greenhouse gases into valuable chemical feedstock. Silica supported bimetallic catalysts with constant metal loading but varying Ni/Co ratios ($x_{Ni} = 1$, 0.8, 0.6, 0.5, 0.4, 0.2, 0) were produced via spray-drying for the application in DRM, aiming at the identification of compositions with superior activity. In this study, building block particles refer to an inert framework, supporting the catalyst. The elemental distribution of Si, Ni, and Co within such building block particles was evaluated using scanning transmission electron microscopy. Additionally, X-ray diffraction and temperature-programmed reduction experiments confirmed that Ni and Co initially exist in an oxidic state within the SiO_2 framework after production and later transform into an alloyed metallic state upon reduction with hydrogen, as confirmed by X-ray photoelectron spectroscopy. A systematic comparison of the activity over a temperature range (323–1150 K) was performed using temperature scanning measurements. The highest intrinsic activity was found with the bimetallic $Ni_{40}Co_{60}$ particles.

Introduction

Synthesis gas, a mixture of hydrogen and carbon monoxide, can be produced by three catalyzed reactions: (i) steam methane reforming, (ii) partial oxidation of methane, and (iii) dry reforming of methane (DRM).[1,2] Especially the latter reaction (see Eq. (1)) has gained much attention in the last decades since it converts two greenhouse gases into a valuable chemical feedstock.

$$CO_2 + CH_4 \rightleftharpoons 2\,CO + 2\,H_2 \quad \Delta H^0_{298} = 247\ \mathrm{kJ\,mol^{-1}} \tag{1}$$

This reaction is an excellent approach to convert also small sources of CH_4 to syngas with a low stoichiometric CO/H_2 ratio.[3,4]

Ni-based catalysts are beneficial for competitive DRM reactors because they are inexpensive and have a catalytic performance comparable to noble metals.[5] However, Ni-based catalysts are prone to coke formation during the endothermic DRM reaction.[6,7] The reaction temperatures typically exceed 1000 K, which leads to sintering. Larger Ni crystals increase the tendency for coke formation even further.[8–10] In one of our studies, carbonaceous deposits were recognized in the axial and radial direction of a packed-bed of spherical Ni/Al_2O_3 catalysts.[11]

Bimetallic Ni-X-catalysts show a tremendous potential to increase the coking and sintering resistance while being cost-effective and efficient.[12–14] Furthermore, the potential application of bimetallic catalysts in inductively heated reactors, where one metal is predominantly catalytically active while the other acts as a heating susceptor, recently gained attention.[15,16] The synergistic effects between Ni and the second metal X, including noble metals (e.g., Pt, Ru, Ir) and transition metals (e.g., Fe, Co, Cu) have recently been reviewed.[17,18] The chemical properties of bimetallic catalysts can be tailored depending on several parameters, such as relative composition, preparation method, interaction of the metals, and particle morphology.[19,20] Since many catalysts are supported onto substrates, the metal-support-interaction affects the overall catalytic performance and stability.[21] Co is one of the most prominent early transition metals for bimetallic Ni catalysts.[14,17] The similar electronic configuration of Co and Ni eases the formation of bimetallic nanoparticles.[22] Co shows a stronger affinity for oxygen species in the DRM. In contrast, Ni exhibits an affinity for adsorbates binding through carbon. Thus, the combination can lead to bimetallic catalysts that suppress metal oxidation and coke formation.[23] Alumina-supported Ni, Co and bimetallic Ni-Co

[a] G. Küchen,[+] Prof. Dr. T. Turek
Institute of Chemical and Electrochemical Process Engineering, Clausthal University of Technology, Leibnizstraße 17, 38678 Clausthal-Zellerfeld, Germany

[b] V. Olszok,[+] Prof. Dr. A. P. Weber
Institute of Particle Technology, Clausthal University of Technology, Leibnizstraße 19, 38678 Clausthal-Zellerfeld, Germany

[c] Dr. B. Kreitz
School of Engineering, Brown University, 184 Hope Street, Providence, 02912 Rhode Island, USA

[d] Dr. C. Mahr, Prof. Dr. A. Rosenauer
Institute of Solid State Physics, University of Bremen, Otto-Hahn-Allee 1, 28359 Bremen, Germany

[e] Prof. Dr. G. D. Wehinger
Institute of Chemical Process Engineering, Karlsruhe Institute of Technology, Kaiserstraße 12, 76131 Karlsruhe, Germany
E-mail: gregor.wehinger@kit.edu

[+] These authors contributed equally.

Supporting information for this article is available on the WWW under https://doi.org/10.1002/cctc.202400371

catalysts were studied with varying metal ratios.[24] Catalysts with a high Co loading performed best with respect to activity and stability. Contrarily, Sengupta et al.[25] studied alumina-supported Ni-Co catalysts for DRM and observed highest turnover frequencies (TOF) for Ni/Co ratios of 3. These catalysts also had the maximum coke deposited. Small and uniform Ni-Co alloy particles supported on SiO_2 were derived with a hydrothermal method, leading to a high activity for a Ni/Co ratio of 9 with little coking. While the addition of small amounts of Co improves the activity, too much Co results in a reduced activity, even below that of a monometallic Ni catalyst.[17] This overview shows that the activity of bimetallic Ni-Co for DRM is highly dependent on the Ni/Co ratio and on the support.

An elegant way to tailor nanoparticles with well-defined properties is via spray-drying, which is simple, continuous, efficient, and fast.[26,27] Spray-drying a colloidal nanoparticle suspension with dissolved metal nitrates allows to define the pore size, surface area, metal particle size, and metal loading. In our previous works, spray-dried Co and Ni nanoparticle catalysts supported on porous SiO_2 and Al_2O_3, so-called "building blocks", were synthesized.[28,29] The tailored Ni catalysts were successfully used for the CO_2 methanation.[30,31] The metal nanoparticle size was adjusted with various temperatures and duration of a subsequent heat treatment, resulting in typical sizes of 2 nm to 15 nm.[29] Other research groups synthesized multi-component alloyed nanoparticles with spray-drying.[32,33]

In the present study, seven catalysts with varying Ni/Co ratios were produced via spray-drying and investigated with physical and chemical characterization techniques. The catalysts were characterized with a range of physical and imaging techniques to gain valuable insights into catalyst morphology and composition. Temperature-programmed reduction measurements allowed to identify involved oxide species. Catalyst activities were evaluated using a transient temperature scanning methodology, which delivers continuous conversion profiles over the whole temperature range. Preliminary experiments indicate the feasible utilization of spray-dried Ni/Co catalysts in inductively heated DRM reactors, where Ni is the catalytically active component, while Co acts as the heating susceptor.

Results and Discussion

Physical Characterization

Electron microscopy analyses were conducted for the investigation of the elemental distribution within a single catalyst particle. Figure 1a depicts the HAADF scan and Figure 1b the elemental distribution of Si, Co, and Ni, respectively. From Figure 1a, it can be seen that a homogeneous distribution of Ni and Co is apparent, as the dark field micrograph relates to elements with a high atomic number. Furthermore, the elemental mapping for Si, Co, and Ni in Figure 1b (EDXS) shows a uniform distribution of the elements as no green or red color (representing Ni or Co) is dominating. A homogeneous mixture of Ni and Co would appear yellow. A different pattern is observed for smaller particles, which were examined at a higher magnification (Figure 2a and b). In the HAADF micrograph, a certain hetero-structure is apparent as the spherical SiO_2 primary particles incorporate small and brightly appearing fractions in the intermediate spaces between adjacent SiO_2 particles. The smaller particles can be attributed to the catalytically active component since a higher HAADF signal correlates to a higher atomic number ($Z_{Si}=14$, $Z_{Co}=27$, $Z_{Ni}=28$). This observation is supported by the results from the elemental mapping (micrograph Figure 2b). Ni and Co do not emerge as perfectly mixed phases after particle synthesis and calcination, indicated by green and red colors in the elemental mapping of the EDXS scans. However, a homogeneous mixture of Ni and Co would appear as yellow, which can be seen as well. With respect to the resolution of the used STEM, it can be stated that a Janus-like morphology has formed, which establishes through a Ni-rich part connected to a Co-rich portion.

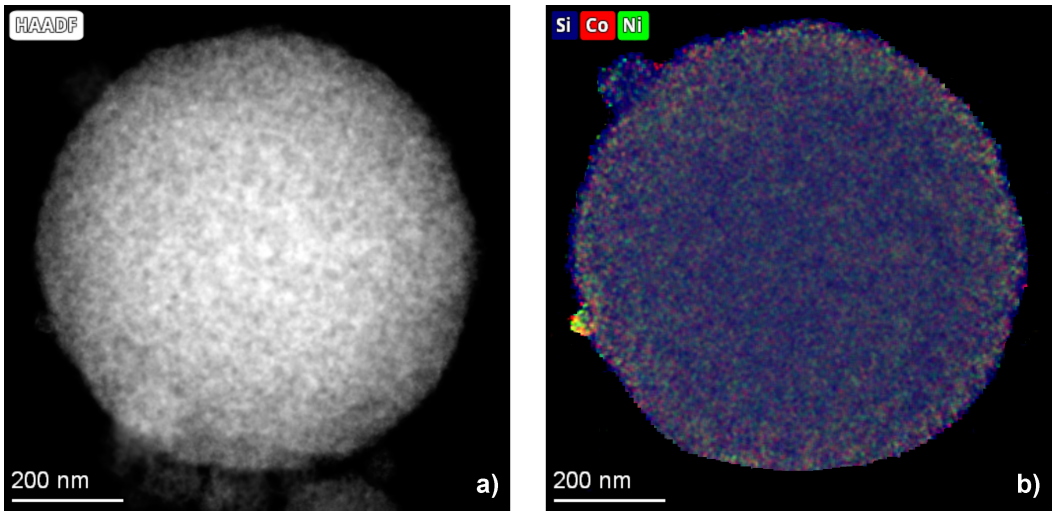

Figure 1. STEM of a large catalyst particle ($Ni_{50}Co_{50}$) after synthesis and subsequent calcination: a) HAADF, b) EDXS. Both micrographs show a homogeneous distribution of Ni and Co within a SiO_2 building block.

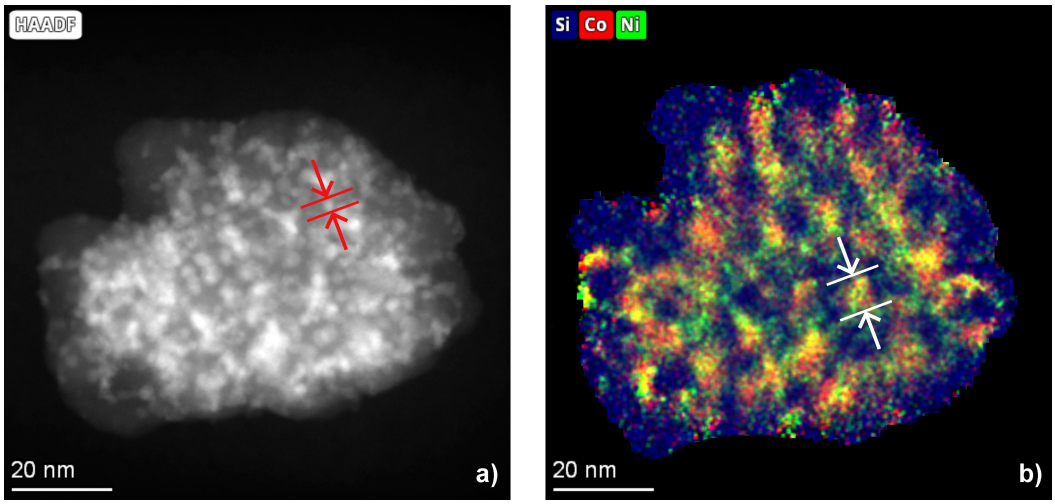

Figure 2. STEM of a small catalyst particle ($Ni_{50}Co_{50}$) after synthesis and subsequent calcination: a) HAADF, b) EDXS. The elemental mapping at a higher magnification reveals a hetero-structure of Ni and Co within a SiO_2 building block. The arrows indicate the size of a metal nanoparticle.

By comparing Figure 2a and b, the substructure of each bimetallic catalyst particle becomes noticeable, indicating that one Ni-Co nanoparticle ($d = 7$ nm, standard deviation $SD =$ 1.2 nm, white arrows) consists of even smaller nanoparticles ($d = 2.8$ nm, $SD = 0.4$ nm, red arrows). The geometric mean diameter of spray-dried building block nanoparticles is 423 nm with a geometric standard deviation factor of 2.09. Due to the spray-drying process, the metal nitrates decompose into metal oxides. A later reduction under hydrogen can change the geometric arrangement of Ni and Co atoms due to metal/metal alloying steps instead of metal oxide/metal oxide mixing. To verify this hypothesis, 15 mg of catalyst powder were subjected to a complete DRM procedure (323 K to 1150 K), including reduction, cooling and passivation. The effect of these process steps on the elemental distribution within a building block particle can be seen in Figure 3. The HAADF micrograph (Figure 3a) indicates separated and bright particles that can be identified as catalytically active sites. During reduction, the oxidic Ni-Co particles vanished and formed spherically sintered bimetallic particles with $d = 7.0$ nm ($SD = 1.6$ nm). The assumption of a bimetallic alloy can be validated by considering the elemental distribution (see Figure 3b). Bright yellow spherical regions rather than separated green/red regions indicate a homogeneous Ni-Co alloy. XPS analyses of a reduced and passivated sample confirmed the formation of an alloyed phase since metallic and oxidic Ni and Co can be identified, leading to the assumption that both metals are present at the surface of the particles. Figure S5 shows the spectra of binding energies for Ni and Co with main peaks around 852.6 eV and 778.1 eV, respectively, according to Biesinger et al.[34] In combination, both analytics demonstrate that the bulk (from STEM-EDXS) and the surface (from XPS) appear homogeneously alloyed. However, it has to be kept in mind that all STEM-EDXS measurements represent two-dimensional projections of the sample and that electron microscopy provides restricted statistics due to a limited number of investigated particles. Nevertheless, the presented micrographs depict the most frequently occurring morphology of building block particles. Overall, it has been

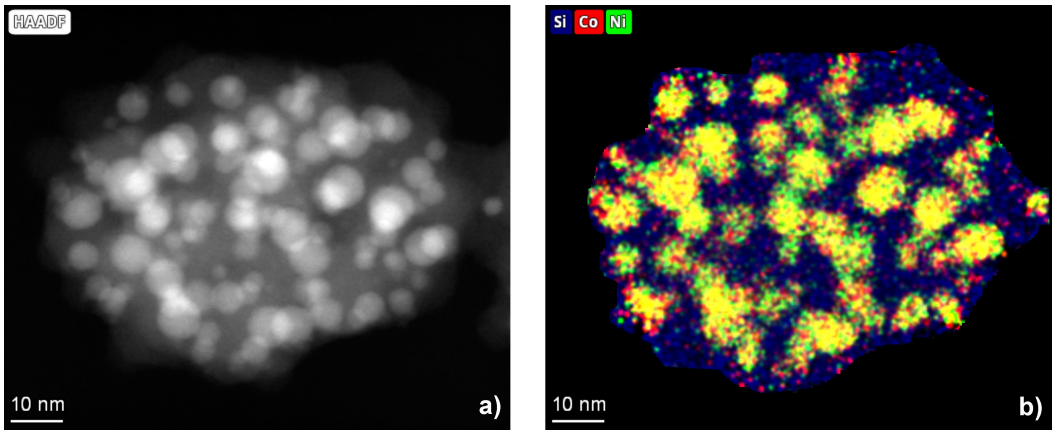

Figure 3. STEM of a small catalyst particle ($Ni_{50}Co_{50}$) after DRM and subsequent passivation by oxygen titration: a) HAADF, b) EDXS. The elemental mapping displays homogeneously alloyed Ni-Co sites.

demonstrated that the spray-drying synthesis yielded SiO_2 building blocks that incorporate finely dispersed but initially non-homogeneously mixed metal oxides from nickel and cobalt. For discussion of the relation between catalytic activity and catalyst morphology, the homogeneously alloyed and sintered particle morphologies have to be taken into account, which appears after reduction.

Figure 4 displays the recorded diffractograms obtained from XRD. All diffractograms have in common that a relatively broad reflex appears at a diffraction angle of 22.3° representing the 8 nm SiO_2 primary particles that create the framework for incorporated mono- and bimetallic particles. The bottom profile refers to the highest Co loading (Co_{100}) and the top profile to the Co-free system (Ni_{100}), respectively. For pure nickel oxide (NiO), characteristic reflexes at 37.2°, 43.3°, 62.9°, 75.2°, and 79.3° appear, indicating that the conversion of nickel nitrate to nickel oxide is complete.[35] An entire precursor conversion becomes noticeable for Co-rich powders as pure cobalt oxide shows reflexes at 31.5°, 37.0°, 44.9°, 59.4°, and 65.4° that can be solely attributed to Co_3O_4.[36] Nevertheless, a gradual peak shift occurs for bimetallic systems at diffraction angles between 62.8° and 65.5°, pointing at a more Ni-like behavior for Ni-rich catalyst particles. A gradual peak shift in dependence of the Ni/Co ratio could also be explained by the variable stoichiometry of a newly formed mixed phase ($Co_{3-x}Ni_xO_4$). Such bimetallic oxides, unfortunately, exhibit a diffraction behavior similar to the monometallic oxides NiO and Co_3O_4, which makes a clear identification of a newly formed bimetallic oxide difficult.[37]

Figure 4 also includes one diffractogram of a reduced and passivated bimetallic catalyst (blue curve). The as-synthesized catalyst powder was reduced under pure hydrogen at 723 K for 45 min and passivated with O_2 by pulse titration prior to XRD offline analysis. The oxidic character of the catalytically active material vanished, which can be clearly seen by the appearance of a reflex at 44.5°, representing metallic Ni and Co. The observed material behavior of the reduced sample coincides with the conclusions drawn from the STEM-EDXS and XPS analyses that the active component consists of a homogeneous Ni-Co alloy.

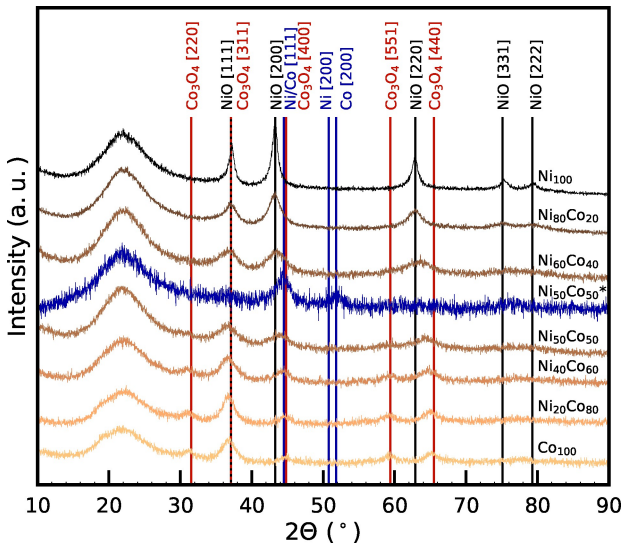

Figure 4. X-ray diffractograms of catalyst particles after synthesis and subsequent calcination. The blue curve is the $Ni_{50}Co_{50}$ sample, which was reduced and passivated.

Temperature-Programmed Reduction

Figure 5 shows the temperature-programmed reduction (TPR) profiles of all mono- and bimetallic catalysts. The TPR profiles of the monometallic samples are displayed at the top and bottom of Figure 5a. These are discussed in greater detail, followed by an elaboration of the TPR profiles of the bimetallic Ni-Co catalysts. The latter show systematic shifts of peak locations and intensities, which can be derived from the spectra of the monometallic samples. TPR spectra are deconvoluted by fitting three to six Gaussian profiles to the recorded spectra highlighting different reduction reactions.

The Ni_{100} catalyst shows three distinctive peaks: a low-temperature shoulder (LT shoulder) at 583 K, the main peak (Ni main) at 628 K and the high-temperature (HT) shoulder at 723 K. The LT shoulder corresponds to the decomposition of Ni^{3+} oxides (Ni_2O_3) which can form during the decomposition of $Ni(NO_3)_2$ in H_2 atmospheres.[38] This decomposition was evidenced by Mile et al.[39] and Luisetto et al.,[40] who located the peak maximum at around 525 K. The broad main peak results from the reduction of bulk NiO, which weakly interacts with the silica support.[39] The HT shoulder at 723 K cannot be attributed to a specific reduction reaction with certainty. This peak could either be the reduction of strongly interacting small NiO particles, the occurrence of particles in which SiO4 groups are incorporated into the NiO lattice,[41,42] or with 1:1 Ni phyllosilicates.[38,42–44]

The monometallic Co_{100} catalyst also shows three reduction peaks. A sharp LT peak at 558 K can not be deconvoluted with a single Gaussian function, indicating two parallel occurring reactions. The predominant share of the LT peak corresponds to the reduction of Co^{3+} to Co^{2+} oxides (see Eq. (2)), which is part of the following two-step reduction mechanism.[40,41,45]

$$Co_3O_4 + H_2 \rightarrow 3\,CoO + H_2O \quad (2)$$

$$CoO + H_2 \rightarrow Co + H_2O \quad (3)$$

These reduction steps have been observed at slightly deviating temperatures of 568 K to 573 K previously, which supports the findings of this work.[45,46] Two more significant peaks located at 716 K and 1029 K can be associated with the reduction of Co^{2+} to Co (see Eq. (3)). This behavior differs from TPR spectra of Co catalysts in relevant literature. Typically, only one distinct peak is reported in the range of 723 K to 773 K[40,45] with a long tailing up to 1100 K.[45,46] A possible reason for the tailing can be the occurrence of small CoO particles formed during synthesis or in the first reduction step (Eq. (2)) that interact strongly with the support.[47] Also, the anions of the catalyst precursor can strongly influence the reduction behavior.[48]

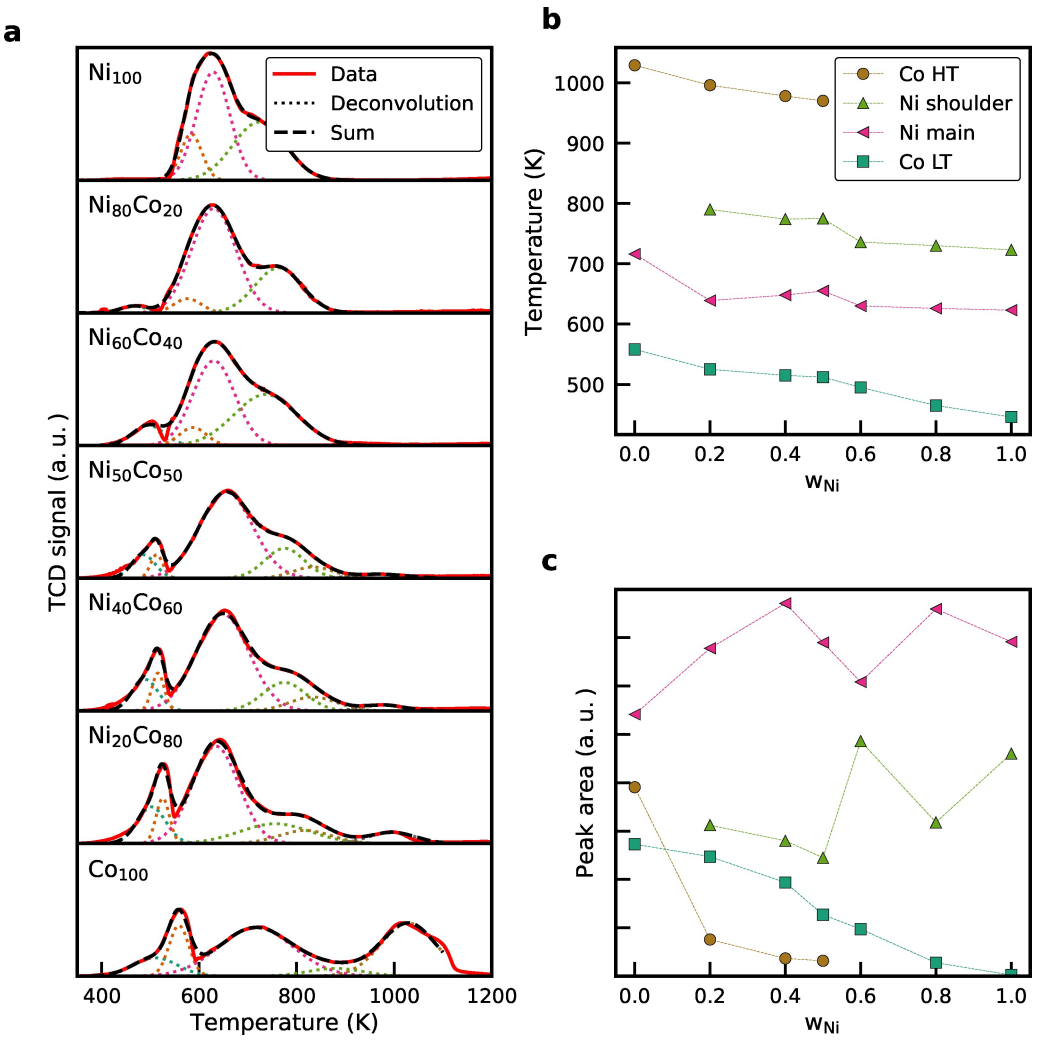

Figure 5. a) Measured temperature-programmed reduction profiles in 10.1 % H_2 in Ar (solid, red). Each spectrum is deconvoluted into three to six Gaussian functions (dashed). Spectra are sorted from Ni-rich to Co-rich catalysts. b) Peak locations and c) peak areas as a function of the Ni content. Conditions: $m_{cat} = 20$ mg, $\beta = 10\ K\,min^{-1}$, $WHSV = 90\ L_N\,g^{-1}\,h^{-1}$.

TPR spectra for the bimetallic samples are depicted in the subplots. The involved oxide species from the bimetallic catalysts can be partly derived from the spectra of the monometallic catalysts. However, that does not account for the reduction peaks of Ni, as these overlay with reduction peaks associated with Co. Figure 5b and c show the peak location and area in dependence of the relative Ni content $x_{Ni} = w_{Ni}/(w_{Ni} + w_{Co})$. The Co LT peak is shifted towards lower temperatures with increasing Ni content and the peak temperatures follow a linear trend similar to the peak areas. Regarding the peak locations, a similar behavior can be observed for the HT Co peak. However, considering the peak areas, a strong decline appears from the Co_{100} to the $Ni_{20}Co_{80}$ catalyst. It can be derived that the reduction of Co oxides is promoted by the occurrence of Ni species.[45] For the other two considered peaks, referred to as Ni main and Ni shoulder, no clear trends in peak shifts and peak areas can be identified, mainly due to the superimposition and the possible formation of mixed phases.[37]

For the comparison with the literature, it has to be considered that the relative peak intensities and peak temperatures can be significantly altered by water in the gas phase. First and foremost, this effect is due to the formation of surface hydrosilicates, which can cover the surface NiO crystals and severely retard the reduction.[49,50] Second, water alters the TCD signals, which are widely spread in experimental setups to measure TPR profiles. Therefore, a water trap (e.g. zeolites) must be used to obtain comparable reduction spectra as done in this work Also, metal/support interactions and the catalyst preparation method need to be considered. For instance, catalyst production via one-pot evaporation induced self-assemble using mesoporous alumina as support can shift the reduction peak of NiO up to around 500 K higher than data obtained in this study.[51]

Temperature-Programmed Desorption

Temperature-programmed desorption was performed to investigate the interaction of CO_2 with the active site motifs. Figure 6 displays the recorded TPD profiles. CO_2 was adsorbed to the reduced catalyst samples at 323 K in flow conditions. All catalysts show a desorption peak of weakly bound CO_2 at low temperatures of 450 K to 490 K. A second, smaller desorption peak evolves at around 600 K to 700 K for all catalyst. For the Ni_{100} catalyst, the desorption of CO_2 begins at 350 K and the maximum is located at around 480 K. The desorption profile shows a local minimum at 560 K and a small high temperature maximum at 600 K.

These two distinct desorption peaks for Ni/SiO_2 were also observed by other researchers.[52–54] Chen et al.[52] located the low temperature desorption peak at 378 K to 398 K and attributed it predominantly to weakly bound CO_2 at surface hydroxyl groups and the high temperature desorption peak was located at 780 K. It was confirmed for this catalyst system that the acidic SiO_2 support does not interact with CO_2.[55] The Co_{100} catalyst shows a similar CO_2 desorption behavior while the high temperature desorption peak is shifted to a higher temperature of around 690 K and is more pronounced compared to the Ni_{100} catalyst indicating a higher share of strongly bound CO_2. The CO_2 adsorption capacity of the bimetallic Ni-Co catalysts exceeds the one of the monometallic catalysts. This observation applies to both, weak and strong binding CO_2. The $Ni_{80}Co_{20}$ catalyst has the highest share of strongly bound CO_2 with a desorption maximum at 600 K. Literature on CO_2-TPD profiles of bimetallic Ni-Co catalysts is scarce. Jia et al.[53] synthesized Ni-Co/SiO_2 catalysts via impregnation and observed only a single desorption peak at lower temperatures. No high temperature desorption peak was observed, which is in contrast to our findings. The metal composition of the catalyst samples can affect the alloy nanoparticle crystal structure, as investigated by Liu et al.[56] In previous work, Kreitz et al.[55] showed through detailed microkinetic modeling of the CO_2 desorption from a multifaceted Ni nanoparticle that the spectrum is a convolution of the desorption from different crystal facets. The lowtemperature desorption peak is presumably desorption from terrace sites, e.g., from the (111) facet. In contrast, the high-temperature peak corresponds to the desorption from under-coordinated sites that bind CO_2 more strongly. The TPD profiles show that the catalyst morphology is strongly affected by the composition of the catalyst. Accordingly, this morphology can impact the activity of the catalyst for the DRM as well.[57]

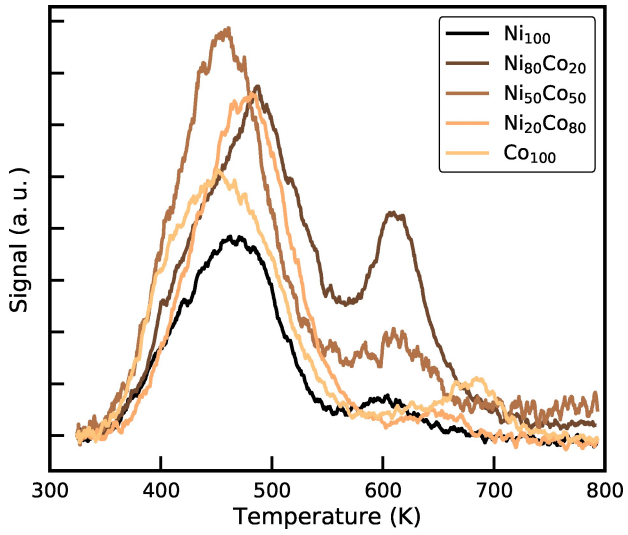

Figure 6. CO_2 temperature-programmed desorption profiles of reduced mono- and bimetallic catalysts after adsorption at 323 K. The profiles are normalized with respect to the metal loading. Conditions: $m_{cat} = 20$ mg, $\beta = 20\ K\,min^{-1}$, $\dot{V}_{Ar} = 30\ mL_N\,min^{-1}$. Adsorption at flow conditions: 5% CO_2 in Ar, $\dot{V}_{CO_2}$ in Ar $= 30\ mL_N\,min^{-1}$ for 60 min.

Activity of the Catalysts

Isothermal steady-state kinetic measurements are a frequently used method to screen the activity of catalytic materials. However, it is time-consuming to reach steady states with this method. Therefore, only a few data points are often mapped in conversion-temperature diagrams. The temperature scanning method used in this study developed by Wojciechowski and Asprey allows obtain a continuous conversion profile by applying a linear temperature ramp.[58,59] We have previously employed this method successfully for the CO_2 methanation over Ni catalysts.[29,30] The obtained conversion profiles for all catalysts are displayed in Figure 7a and the product ratio H_2/CO in Figure 7b.

Preliminary investigations on the heating rate resulted in $20\ K\,min^{-1}$ as the most efficient rate (see Figure S2). The reaction is fast and steady states are attained almost instantaneously during the temperature ramp (see Figure S2). The dashed lines correspond to the equilibrium composition, which was obtained via the minimization of the Gibbs enthalpy using Cantera.[60] Thermochemical properties of the gasphase species were taken from the Active Thermochemical Tables (ATcT).[61] Conversion profiles are reported on a dry basis because of an inaccurate measurement of water with the MS due to partial condensation. Carbon balances are closed to within ±1.5% for all samples over the whole temperature range. The corresponding concentration profiles are depicted in Figure S3. In equilibrium, the formation of the products CO and H_2 sets in at around 550 K and full conversion is reached at ca. 1100 K. At intermediate temperatures, the CO concentration is higher than the H_2 concentration. The H_2/CO ratio reaches approx. 1 at maximum conversion. The measured conversion profiles are well below the equilibrium conversion at high temperatures for all catalysts. This gap was achieved on purpose to identify slight differences in activity between the catalysts. Equilibrium conversions could easily be achieved using a lower *WHSV* or a higher catalyst mass (see Figure S1). The conversion of the Ni_{100} catalyst reaches around 96% with a product ratio of 0.96 at 1100 K. Conversion and product ratio are slightly lower for the $Ni_{80}Co_{20}$ catalyst with 89.4% and 0.94, respectively. This trend continues with decreasing Ni content ($Ni_{50}Co_{50}$, $Ni_{40}Co_{60}$, $Ni_{20}Co_{80}$) and can be attributed to the lower relative Ni loading

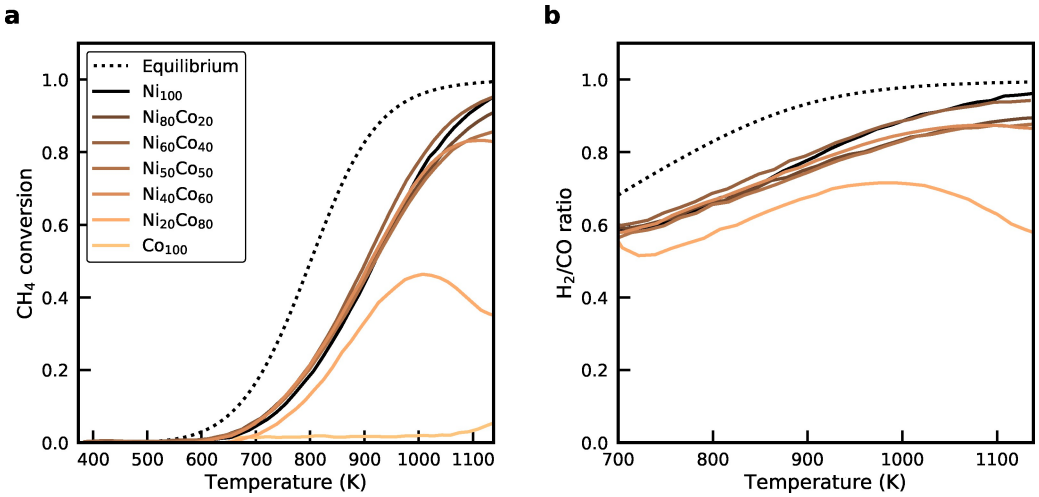

Figure 7. a) CH_4 conversion profiles and b) molar H_2/CO product ratios of all catalysts. Both figures share the same legend. Conditions: $m_{cat} = 12$ mg, $\beta = 20\ K\,min^{-1}$, $WHSV = 1000\ L_N\,g^{-1}\,h^{-1}$.

w_{Ni}. Only the $Ni_{60}Co_{40}$ breaks this observation (95.3 % conversion at a ratio of 0.95), which is probably caused by the higher overall metal loading (13.1 wt %) resulting in a higher activity.

Another trend that evolves with higher Co contents is the formation of conversion maxima, which can already be anticipated for the $Ni_{50}Co_{50}$ catalyst, examining a slight kink at 1000 K. This kink evolves to a plateau with the $Ni_{40}Co_{60}$ catalyst, where a global conversion maximum can be examined at ca. 1050 K. The trend solidifies with the $Ni_{20}Co_{80}$ catalyst, where the maximum is more distinct and occurs at a lower temperature around 1000 K. Only minimal conversion occurs at temperatures larger than 1050 K with the Co_{100} catalyst. The observed behavior can be either ascribed to catalyst deactivation phenomena or to occurring side reactions, like the *reverse Water Gas Shift reaction* (rWGS) or the *Boudouard* reaction. Water was not accurately measured in the utilized setup, so the effect of the rWGS can not be quantified. Temperature-programmed oxidation (TPO) measurements subsequent to the DRM experiments (see Figure S6) showed no significant coke deposits. Therefore, the occurrence of the *Boudouard* reaction is unlikely during the temperature scans. The investigation of deactivation phenomena is not in the focus of this study. However, comparative long-term tests of a pure Ni and a Ni-Co catalyst indicate an improved coking resistance of the bimetallic sample (see Figure S7).

Literature on temperature scanning experiments for DRM is scarce. However, studies using classical steadystate isothermal measurements have been conducted and can be considered for comparison as nearly steady states are supposed to be reached at every temperature increment using the applied temperature scanning method (see Figure S2). The effectiveness of the applied temperature scanning method, especially for screening purposes, becomes apparent from this comparison. Luisetto et al.[40] investigated bimetallic Ni-Co/CeO_2 catalysts (7.5 wt %) and found similar conversions but slightly higher product ratios. Djinovic et al.[62] deposited Ni and Co via homogeneous deposition precipitation at a weight ratio of $Ni_{40}Co_{60}$. Product ratios up to 0.67 were observed at 1073 K with corresponding conversions of around 50 %, which is significantly lower than the conversions seen in this study for comparably loaded catalysts. This deviation is probably due to the choice of support materials, the experimental setup and measurement program, which was designed for long-term studies to resolve coking phenomena. Huang et al.[63] used shell-like silica as a support for 10 wt % nickel and observed full conversion at 1100 K but a product ratio of only 0.75.

Activation Energies and Turnover Frequencies

Reaction rates for the production of CO were calculated at conversions up to 10 %, assuming differential fixed bed conditions. The Arrhenius dependence between the rate of CO formation and temperature for the considered catalyst is depicted in Figure S4. Changes in the slopes are minor between the Ni-rich catalysts to the $Ni_{40}Co_{60}$ catalyst, resulting in activation energies of $74 \pm 4\ kJ\,mol^{-1}$. For the $Ni_{20}Co_{80}$ catalyst, a significantly higher activation energy of $114\ kJ\,mol^{-1}$ is observed due to the considerable lower conversions at the considered temperature. An activation energy for the Co_{100} could not be determined as significant conversions are only detected above 1000 K. A TOF for the $Ni_{60}Co_{40}$ sample could not be calculated, as no adsorption capacity was measured.

Figure 8a summarizes the obtained TOFs. A trend to higher TOFs towards medium Ni contents can be examined. The highest TOF is observed for the $Ni_{40}Co_{60}$ sample with $0.701\ s^{-1}$. From the $Ni_{50}Co_{50}$ to the monometallic Ni catalyst, the TOFs decrease slightly but remain on a level above $0.5\ s^{-1}$. In alignment with the high activation energy, the TOF for the $Ni_{20}Co_{80}$ catalyst is lower than for the other bimetallic samples, but at a comparable level to the Ni_{100} catalyst. Literature data on bimetallic Ni-Co catalysts are considered to establish the significance of the obtained TOFs. It should be noted that TOFs in the literature are predominantly determined at significantly

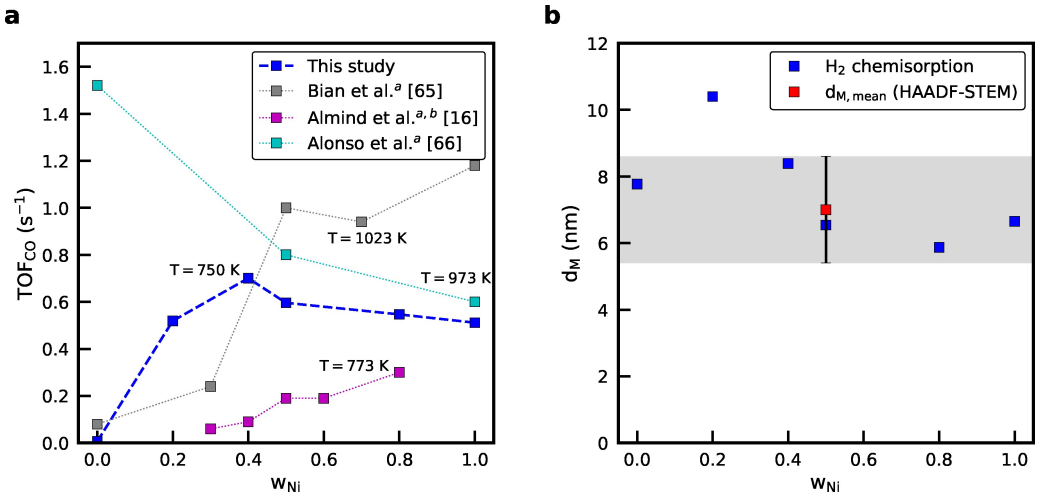

Figure 8. a) TOF_{CO} as a function of the Ni content. Values from the literature are depicted for comparison. Note the different temperatures. For more details see Table S2. b) Mean metal crystal diameter derived from chemisorption measurements as a function of the Ni content (blue) and STEM analysis for a $Ni_{50}Co_{50}$ sample (red). [a] The TOF_{CO} is calculated using correlations of Borodzinski et al.[64] [b] Steam methane reforming.

higher temperatures, which is not feasible with the setup used in this study. In a study from Bian et al.,[65] SiO_2 was used as carrier material in an IWI synthesis process, and reaction rates were determined at harsh conditions ($WHSV = 60\,000\ L_N g^{-1} h^{-1}$, $T = 1023$ K). These authors measured TOFs up to 1.18 s^{-1}. However, the highest TOF is revealed at the monometallic Ni catalyst, which differs clearly from the behavior observed in this work. The mentioned increasing trend was also observed by Almind et al.,[16] who produced bimetallic Ni-Co catalysts on Al_2O_3. Instead of DRM, the TOF was determined for steam methane reforming at 773 K. A defined increase of TOF from low to high Ni contents was examined, but on a substantially lower level than in this work. San-Jose-Alonso et al.[66] also used Al_2O_3 as carrier material, but interestingly found the highest TOF with the monometallic Co catalyst with 1.52 s^{-1}, which steadily decreases to about 0.6 s^{-1} with $w_{Ni} = 1$. Reaction rates were calculated at 973 K, a *WHSV* of 22 000 $L_N g^{-1} h^{-1}$ with an equimolar and non-diluted feed gas composition.[66] These findings and particularly opposing trends in the literature emphasize the delicate effects of the exact procedure during catalyst synthesis and reduction on the resulting activity, which have to be considered for a rigorous evaluation.[67]

The obtained mean crystal sizes d_M for all samples are displayed in Figure 8b. No significant dependence between crystal size and Ni content can be derived from chemisorption experiments suggesting a structure insensitive reaction. The crystal diameter from STEM image analysis of a $Ni_{50}Co_{50}$ sample is in the range of 7.6 ± 1.5 nm. The gray shaded area represents the optically determined crystal size standard deviation based on STEM micrographs. Good agreement is observed between the two methods. This narrow range of diameters is in line with the findings from ICP-OES measurements (see Table 1 for more details) as the overall metal loadings are proven to be in a tight range as well.

Bimetallic Ni-Co catalysts were produced via spray-drying. This continuous technique proves to be an advantageous route for multi-component catalyst preparation, as metal nitrates can be immersed in varying concentrations to the aqueous dispersion of silica according to the intended Ni/Co ratio. Spherical particles with evenly distributed metal oxides within the SiO_2 building blocks were produced. This uniform distribution was evidenced by STEM-EDXS elemental mapping alongside XRD analyses. TPR measurements showed the complete decomposition of the nitrate compounds during calcination. However, after a DRM cycle, evenly distributed and homoge-

Table 1. Summary of measured and calculated properties of the produced catalyst nanoparticles.

Intended composition	Total loading (wt%)	Measured composition	SSA ($m^2 g^{-1}$)	Q_{H_2} ($\mu mol\, g^{-1}$)	a_M ($m^2 g^{-1}$)	d_M (nm)	D (%)
Ni_{100}	12.3	Ni_{100}	222	156.7	12.45	6.65	14.6
$Ni_{80}Co_{20}$	11.7	$Ni_{79.7}Co_{20.3}$	221	171.1	13.45	5.87	17.2
$Ni_{60}Co_{40}$	13.1	$Ni_{58.8}Co_{41.2}$	203	N/A	N/A	N/A	N/A
$Ni_{50}Co_{50}$	11.7	$Ni_{47.5}Co_{52.5}$	208	149.8	12.05	6.54	15.3
$Ni_{40}Co_{60}$	13.6	$Ni_{39.0}Co_{61.0}$	212	135.6	10.92	8.39	12.0
$Ni_{20}Co_{80}$	13.5	$Ni_{19.7}Co_{80.3}$	204	108.4	8.75	10.4	9.64
Co_{100}	12.1	Co_{100}	208	132.4	10.5	7.77	12.9

neously mixed Ni-Co nanoparticles with a mean size of 7.4 nm can be observed within the pores of the support material. Overall, the catalytic activity decreases in accordance to the Ni loading. Only slightly decreasing activities are observed down to the $Ni_{40}Co_{60}$ sample. With lower Ni contents, drastically lower conversions and product ratios are obtained. TOFs are comparable to the literature for all catalysts, except for the Co_{100} sample. Interestingly, the highest TOF is observed for the bimetallic $Ni_{40}Co_{60}$ sample with 0.7 s^{-1}.

A recent and promising application of bimetallic catalysts is induction heating,[15] where one metal is the heating susceptor and the other is catalytically active. Induction heating imposes an alternating magnetic field, where friction between physically rotating nanoparticles generates heat. Superparamagnetic and ferromagnetic nanoparticles show different magnetic loss mechanisms. The latter dissipates energy through hysteresis losses.[68] For high-temperature applications such as DRM, only a few metals show sufficiently high Curie temperatures T_c, which marks the transition from ferromagnetism to paramagnetism; no heating occurs above T_c.[69] Ni has a T_c of 627 K, whereas it is 1494 K for Co and 1043 K for Fe. Preliminary own results underline the suitability of spray-dried bimetallic Ni-Co/SiO_2 catalysts for application in inductively heated reactor systems (see SI). Comprehensive investigations of induction heated DRM are being conducted in the near future and are therefore not the subject of this work.

Conclusions

Active Ni-Co/SiO_2 bimetallic particles with a high specific metal surface area were successfully synthesized in a spray-drying setup, which allows the tailored production of multimetallic catalysts. Electron microscopy analysis revealed a homogenous and finely dispersed Ni-Co mixture within each SiO_2 building block. TPR experiments revealed interactions on the atomic level between both metals, which might also be assumed following the obtained XRD data. A transient screening method was applied to investigate the DRM activity. Pure Ni catalyst to bimetallic $Ni_{40}Co_{60}$ catalysts were identified to be highly active with conversions above 82%. Remarkably high TOFs were found for particles with compositions between $Ni_{80}Co_{20}$ and $Ni_{40}Co_{60}$, while a slight decrease towards the monometallic Ni_{100} catalyst can be observed. Preliminary observations from induction heating experiments verify the potential applicability of spray-dried bimetallic Ni-Co catalysts in induction heating setups. Therefore, future investigations could focus on the magnetic properties, i.e., specific absorption rate, Curie temperature, and longevity of the produced bimetallic catalysts, to further assess their induction heating capabilities.

Experimental

Catalyst Preparation

In this work, a spray-drying setup identical to that used by Martínez et al.[28] was used to produce Ni-Co/SiO_2 bimetallic nanoparticles with a constant total metal loading of 12 wt% and varying Ni/Co ratios. As precursors, $Ni(NO_3)_2 \cdot 6H_2O$ and $Co(NO_3)_2 \cdot 6H_2O$ (Sigma–Aldrich) were used and a colloidal SiO_2 suspension (Köstrosol 0830AS, 8 nm, 30 wt% in H_2O) was utilized as a pre-manufactured SiO_2 dispersion.[28,29] The mixture of colloidal SiO_2, nickel nitrate, and cobalt nitrate was stirred in an ultrasonic bath for 20 min to homogenize all components. The centerpiece of the spray-drying setup is a pneumatic atomizer (AGK 2000, Palas), which was supplied with pressurized, filtered air to finely atomize the prepared metal nitrate silica suspension into a heated tube furnace (T = 673 K). Thermally unstable metal nitrates decompose while passing through the furnace with a mean residence time of 1.6 s, forming a building block particle where Ni-Co oxide compound particles are embedded within a porous silica matrix. Downstream of the furnace, a filter sampled the produced particles, which were then calcined in a muffle oven with air at 673 K for 3 h. The calcination step completes the conversion of the precursor into metal oxides and defines the particle size of the active component by Ostwald ripening, particle migration, and coalescence. This step comes along with a slight increase of the active component particle size.[28]

Physical Characterization

Specific surface areas (SSA) of the produced nanoparticles were measured with BET analysis (ASAP 2020, Micromeritics Instruments Corp.) using N_2 as adsorptive. X-ray diffraction (XRD) was utilized for the crystallographic characterization of the catalyst powders (Empyrean, Malvern Panalytical Ltd., Bragg-Brentano configuration, Cu Kα, λ = 1.5406 Å, 8° min^{-1}). X-ray photoelectron spectroscopy (XPS) was applied to selected samples for catalyst surface investigation by binding energy analysis (VG ESCA Lab MKII (modified), Al Kα). High-angle annular darkfield (HAADF) STEM micrographs and STEM-EDXS maps of particles were acquired in a Thermo Fisher Spectra 300 microscope equipped with a Cs-corrector for the probe forming system, an X-FEG, and a SuperX EDXS detector operated at an acceleration voltage of 300 kV. Samples for electron microscopy were prepared on a copper carbon grid. If required, reduced samples were passivated via surface titration with 20 pulses of 1.037 mL synthetic air in Ar at 323 K in the BelCat-M (MicrotracBEL Corp.), following the procedure outlined by Friedland et al.[70]

Chemical Characterization

Temperature-programmed reduction (TPR) experiments were conducted in a BelCat-M catalyst analyzer. The device contains a concentric quartz reactor operated at ambient pressure, which is placed inside a furnace (see Friedland et al.[70] for further details). 20 mg of the catalyst were first degassed at 373 K for 60 min in an Ar atmosphere to eliminate adsorbed species. The TPR measurements were conducted in 10.1% H_2 in Ar at a volumetric flow rate of 30 $mL_N min^{-1}$ with a linear temperature ramp of 10 K min^{-1} from 323 K to 1200 K. Hydrogen consumption was analyzed using a thermal conductivity detector (TCD). The produced water was removed prior to the TCD through a molecular sieve with a pore size of 3 Å. Temperature-programmed desorption (TPD) measurements of CO_2 were conducted in the BelCat-M device and the desorbed gases were analyzed in a mass spectrometer (GAM200, InProcessInstruments). A mixture of 5% CO_2 in Ar was fed through

the catalyst bed for 60 min at 323 K. The catalyst was then flushed with Ar for 15 min. A linear temperature ramp of 20 K min^{-1} up to 773 K was applied for the TPD. Desorbed CO_2 was measured at $m/z = 44$ achieving a cycle time of 0.8 s.

Metal dispersion D, metal surface area a_M, and crystallite size d_M were determined using H_2 pulse adsorption measurements at 323 K in the BelCat-M, which is equipped with a 1.0125 cm^3 sample loop containing a gas amount of about 40 μmol at ambient temperature and pressure. 20 mg of the sample were reduced at 723 K for 90 min in pure H_2 and then flushed at 773 K in Ar for 30 min to desorb all adsorbed species from the metal surface.

20 pulses with 10.1 % H_2 in Ar were induced with a frequency of 1 min^{-1} as described by Friedland et al.[70] The measured pulse signals allow to derive the adsorbed amount of hydrogen Q_{H_2} and the metal properties according to:

$$D = \frac{Q_{H_2} \tilde{M}_M s}{m_s w_M} \tag{4}$$

$$a_M = \frac{Q_{H_2} N_A o_M s}{m_s} \tag{5}$$

$$d_M = \frac{6 w_M}{\rho_M a_M} \tag{6}$$

A spherical shape of the particles was assumed,[71] where s accounts for the dissociative adsorption stoichiometry of H_2 on metal sites, m_s is the sample mass, N_A is the Avogadro constant and o_M corresponds to the surface area of a metal atom, for which $o_{Ni} = 6.51$ Å^2 (fcc) and $o_{Co} = 6.59$ Å^2 (fcc) are used.[72] The overall metal loading reads as $w_M = w_{Ni} + w_{Co}$. In bimetallic systems, physical properties (M_M, o_M, ρ_M) are assumed as arithmetic means of the corresponding values of Ni and Co respectively (see Equations S1–S3).

DRM Measurements

DRM measurements were conducted in the BelCat-M connected to a mass spectrometer (MS). 12 mg of the sample were placed in a sample tube and fixed with quartz wool (see Friedland et al.)[70] to investigate the activity of the catalysts. The samples were initially reduced in pure H_2 at 723 K for 75 min. Temperature scanning experiments[29] were performed with a stoichiometric mixture of CO_2 (5.03 %) and CH_4 (5.00 %) in Ar as internal standard and dilutant, which was fed with a constant volumetric flow rate ($WHSV$ = 1000 $L_N g^{-1} h^{-1}$) through the catalyst bed. The temperature was raised from 373 K to 1200 K with a linear heating rate of 20 K min^{-1}. A thermocouple was placed directly above the catalyst bed. The product gas composition was analyzed with the MS, which was calibrated for CO_2, CH_4, CO, H_2, and Ar using certified calibration gas mixtures. A measurement time of 0.9 s per cycle was achieved.

The CO_2 conversion X_{CO_2} was calculated based on the outlet gas composition with Ar as an internal standard using Eq. (7).

$$X_{CO_2} = 1 - \frac{x_{CO_2}^{out} x_{Ar}^{in}}{x_{CO_2}^{in} x_{Ar}^{out}} \tag{7}$$

Reaction rates were calculated at 750 K where the conversion for all samples was below 10 %, assuming differential fixed-bed conditions. The CO formation rate was calculated with:

$$r_{CO} = \alpha x_{CO}^{out} \frac{\dot{V}_N^{in} p_N}{m_s R T_N} \tag{8}$$

where the volume expansion during the reaction is expressed by α based on the internal standard Ar. Together with the amount of adsorbed hydrogen Q_{H_2} and the adsorption stoichiometry s, it was possible to calculate the turnover frequency TOF:

$$TOF_{CO} = \frac{r_{CO}}{s Q_{H_2}} \tag{9}$$

Supporting Information

A supplementary information is available online.

Acknowledgements

The authors gratefully acknowledge the German Research Foundation (DFG) for funding within program SPP 2289 "Hetero-Aggregates" under grants WE2331/30-1, RO2057/17-1, and MA3333/25-1. Bjarne Kreitz acknowledges financial support from the Alexander von Humboldt Foundation. The authors also thank the Institute of Mineral and Waste Processing, Waste Disposal and Geomechanics of Clausthal University of Technology for ICP-OES analyses and the Clausthal Center for Material Technology for XPS measurements. Open Access funding enabled and organized by Projekt DEAL.

Conflict of Interests

The authors declare no competing financial interest.

Data Availability Statement

The data that support the findings of this study are available from the corresponding author upon reasonable request.

Keywords: dry reforming of methane · spray-drying · supported catalysts · nanoparticles · temperature scanning experiments

[1] M. C. J. Bradford, M. A. Vannice, *Catal. Rev.* **1999**, *41*, 1.
[2] J. R. Rostrup-Nielsen, *Catal. Today* **2000**, *63*, 159.
[3] M. Usman, W. Wan Daud, H. F. Abbas, *Renewable Sustainable Energy Rev.* **2015**, *45*, 710.
[4] N. A. K. Aramouni, J. G. Touma, B. A. Tarboush, J. Zeaiter, M. N. Ahmad, *Renewable Sustainable Energy Rev.* **2018**, *82*, 2570.
[5] M. Yusuf, A. S. Farooqi, L. K. Keong, K. Hellgardt, B. Abdullah, *Chem. Eng. Sci.* **2021**, *229*, 116072.
[6] O. Muraza, A. Galadima, *Int. J. Energy Res.* **2015**, *39*, 1196.
[7] S. Arora, R. Prasad, *RSC Adv.* **2016**, *6*, 108668.
[8] J. W. Han, J. S. Park, M. S. Choi, H. Lee, *Appl. Catal. B* **2017**, *203*, 625.
[9] C. Vogt, J. Kranenborg, M. Monai, B. M. Weckhuysen, *ACS Catal.* **2020**, *10*, 1428.
[10] J. F. M. Simons, T. J. de Heer, R. C. J. van de Poll, V. Muravev, N. Kosinov, E. J. M. Hensen, *J. Am. Chem. Soc.* **2023**, *145*, 20289, pMID: 37677099.

[11] G. D. Wehinger, M. Kraume, V. Berg, O. Korup, K. Mette, R. Schlögl, M. Behrens, R. Horn, *AIChE J.* **2016**, *62*, 4436.
[12] Z. Qin, J. Chen, X. Xie, X. Luo, T. Su, H. Ji, *Environ. Chem. Lett.* **2020**, *18*, 997.
[13] X. Fan, Z. Liu, Y.-A. Zhu, G. Tong, J. Zhang, C. Engelbrekt, J. Ulstrup, K. Zhu, X. Zhou, *J. Catal.* **2015**, *330*, 106.
[14] I. V. Yentekakis, P. Panagiotopoulou, G. Artemakis, *Appl. Catal. B* **2021**, *296*, 120210.
[15] A. I. Stankiewicz, H. Nigar, *React. Chem. Eng.* **2020**, *5*, 1005.
[16] M. R. Almind, M. G. Vinum, S. T. Wismann, M. F. Hansen, S. B. Vendelbo, J. S. Engbæk, P. M. Mortensen, I. Chorkendorff, C. Frandsen, *ACS Appl. Nano Mater.* **2021**, *4*, 11537.
[17] Z. Bian, S. Das, M. H. Wai, P. Hongmanorom, S. Kawi, *ChemPhysChem* **2017**, *18*, 3117.
[18] J. Zhang, H. Wang, A. Dalai, *J. Catal.* **2007**, *249*, 300.
[19] S. De, J. Zhang, R. Luque, N. Yan, *Energy Environ. Sci.* **2016**, *9*, 3314.
[20] K. D. Gilroy, A. Ruditskiy, H.-C. Peng, D. Qin, Y. Xia, *Chem. Rev.* **2016**, *116*, 10414.
[21] T. W. van Deelen, C. Hernández Mejía, K. P. de Jong, *Nat. Catal.* **2019**, *2*, 955.
[22] Z. Wu, B. Yang, S. Miao, W. Liu, J. Xie, S. Lee, M. J. Pellin, D. Xiao, D. Su, D. Ma, *ACS Catal.* **2019**, *9*, 2693.
[23] C. Bartholomew, G. Weatherbee, G. Jarvi, *Chem. Eng. Commun.* **1980**, *5*, 125.
[24] D. San-José-Alonso, J. Juan-Juan, M. Illán-Gómez, M. Román-Martínez, *Appl. Catal. A* **2009**, *371*, 54.
[25] S. Sengupta, K. Ray, G. Deo, *Int. J. Hydrogen Energy* **2014**, *39*, 11462.
[26] L. Gradon, R. Balgis, T. Hirano, A. M. Rahmatika, T. Ogi, K. Okuyama, *J. Aerosol Sci.* **2020**, *149*, 105608.
[27] N. Pegios, V. Bliznuk, S. Prünte, J. M. Schneider, R. Palkovits, K. Simeonov, *RSC Adv.* **2018**, *8*, 606.
[28] A. Martínez Arias, A. P. Weber, *J. Aerosol Sci.* **2019**, *131*, 1.
[29] B. Kreitz, A. Martínez Arias, J. Martin, A. Weber, T. Turek, *Catalysts* **2020**, *10*, 1410.
[30] B. Kreitz, K. Sargsyan, K. Blöndal, E. J. Mazeau, R. H. West, G. D. Wehinger, T. Turek, C. F. Goldsmith, *JACS Au* **2021**, *1*, 1656.
[31] B. Kreitz, G. D. Wehinger, C. F. Goldsmith, T. Turek, *ChemCatChem* **2022**, *14*.
[32] C. Yao, H. Xu, A. Li, J. Li, F. Pang, P. Zhao, J. He, W. Yi, Y. Jiang, L. Huang, *RSC Adv.* **2020**, *10*, 3579.
[33] Y. Yang, B. Song, X. Ke, F. Xu, K. N. Bozhilov, L. Hu, R. Shahbazian-Yassar, M. R. Zachariah, *Langmuir* **2020**, *36*, 1985.
[34] M. C. Biesinger, B. P. Payne, A. P. Grosvenor, L. W. Lau, A. R. Gerson, R. S. Smart, *Appl. Surf. Sci.* **2011**, *257*, 2717.
[35] Z. Wei, H. Qiao, H. Yang, C. Zhang, X. Yan, *J. Alloys Compd.* **2009**, *479*, 855.
[36] D. D. M. Prabaharan, K. Sadaiyandi, M. Mahendran, S. Sagadevan, *Appl. Phys. A: Mater. Sci. Process.* **2017**, *123*, 1.
[37] L. J. Cardenas Flechas, A. M. Raba Paéz, M. Rincon Joya, *Dyna* **2020**, *87*, 184.
[38] S.-C. Ho, T.-C. Chou, *Ind. Eng. Chem. Res.* **1995**, *1995*, 2279.
[39] B. Mile, D. Stirling, M. A. Zammit, A. Lovell, *J. Catal.* **1998**, *1988*, 217.
[40] I. Luisetto, S. Tuti, E. Di Bartolomeo, *Int. J. Hydrogen Energy* **2012**, *37*, 15992.
[41] Q. Liu, B. Bian, J. Fan, J. Yang, *Int. J. Hydrogen Energy* **2018**, *43*, 4893.
[42] J. L. Lifeng Zhang, Y. Chen, *J. Chem. Soc. Faraday Trans.* **1992**, *1992*, 2075.
[43] P. Burattin, M. Che, C. Louis, *J. Phys. Chem. B* **2000**, *104*, 10482.
[44] C. Louis, Z. C. Xing, M. Che, *J. Phys. Chem.* **1993**, *1993*, 5703.
[45] P. Liu, B. Zhao, S. Li, H. Shi, M. Ma, J. Lu, F. Yang, X. Deng, X. Jia, X. Ma, X. Yan, *Ind. Eng. Chem. Res.* **2020**, *59*, 5.
[46] B. Zhao, P. Liu, S. Li, H. Shi, X. Jia, Q. Wang, F. Yang, Z. Song, C. Guo, J. Hu, Z. Chen, X. Yan, X. Ma, *Appl. Catal. B* **2020**, *278*, 119307.
[47] H. Romar, A. H. Lillebo, P. Tynjala, T. Hu, A. Holmen, E. A. Blekkan, U. Lassi, *J. Mater. Sci. Res.* **2016**, *5*, 39.
[48] M. Mehrbod, M. Martinelli, C. D. Watson, D. C. Cronauer, A. J. Kropf, G. Jacobs, *Reactions* **2021**, *2*, 129.
[49] J. Zielifiski, *Catal. Lett.* **1995**, *1995*, 47.
[50] A. M. Hilmen, D. Schanke, K. F. Hanssen, A. Holmen, *Appl. Catal. A* **1999**, *1999*, 169.
[51] L. Xu, X. Lian, M. Chen, Y. Cui, F. Wang, W. Li, B. Huang, *Int. J. Hydrogen Energy* **2018**, *43*, 17172.
[52] X. Chen, S. Ullah, R. Ye, C. Jin, H. Hu, F. Hu, Y. Peng, Z.-H. Lu, G. Feng, L. Zhou, R. Zhang, *Energy Fuels* **2023**, *37*, 3865.
[53] C. Jia, Y. Dai, Y. Yang, J. W. Chew, *Int. J. Hydrogen Energy* **2019**, *44*, 13443.
[54] X. Zhang, W.-j. Sun, W. Chu, *J. Fuel Chem. Technol.* **2013**, *41*, 96.
[55] B. Kreitz, G. D. Wehinger, C. F. Goldsmith, T. Turek, *J. Phys. Chem. C* **2021**, *125*, 2984.
[56] P. Liu, D. Chen, Q. Wang, P. Xu, M. Long, H. Duan, *J. Phys. Chem. Solids* **2020**, *137*, 109194.
[57] W. Chen, T. F. Kimpel, Y. Song, F.-K. Chiang, B. Zijlstra, R. Pestman, P. Wang, E. J. M. Hensen, *ACS Catal.* **2018**, *8*, 1580.
[58] B. Wojciechowski, *Catal. Today* **1997**, *36*, 167.
[59] S. Asprey, N. Rice, B. Wojciechowski, *Catal. Today* **1997**, *36*, 209.
[60] D. G. Goodwin, H. K. Moffat, I. Schoegl, R. L. Speth, B. W. Weber, Cantera: An Object-oriented Software Toolkit for Chemical Kinetics, Thermodynamics, and Transport Processes, https://www.cantera.org **2023**, version 2.6.0.
[61] B. Rusic, D. H. Bross, Active Thermochemical Tables (ATcT) Values Based on ver. 1.124 of the Thermochemical Network **2023**, accessed 05/02/2023.
[62] P. Djinović, I. G. Osojnik Črnivec, B. Erjavec, A. Pintar, *Appl. Catal. B* **2012**, *125*, 259.
[63] F. Huang, R. Wang, C. Yang, H. Driss, W. Chu, H. Zhang, *J. Energy Chem.* **2016**, *25*, 709.
[64] A. Borodziński, M. Bonarowska, *Langmuir* **1997**, *13*, 5613.
[65] Z. Bian, S. Kawi, *J. CO_2 Util.* **2017**, *18*, 345.
[66] D. San-José-Alonso, J. Juan-Juan, M. J. Illán-Gómez, M. C. Román-Martínez, *Appl. Catal. A* **2009**, *371*, 54.
[67] S. Xie, X. Zhang, Q. Tu, B. Shi, Y. Cui, C. Chen, *ACS Omega* **2018**, *3*, 13335.
[68] W. Wang, G. Tuci, C. Duong-Viet, Y. Liu, A. Rossin, L. Luconi, J.-M. Nhut, L. Nguyen-Dinh, C. Pham-Huu, G. Giambastiani, *ACS Catal.* **2019**, *9*, 7921.
[69] J. Marbaix, N. Mille, L.-M. Lacroix, J. M. Asensio, P.-F. Fazzini, K. Soulantica, J. Carrey, B. Chaudret, *ACS Appl. Nano Mater.* **2020**, *3*, 3767.
[70] J. Friedland, B. Kreitz, H. Grimm, T. Turek, R. Güttel, *ChemCatChem* **2020**, *12*, 4373.
[71] J. A. Dumesic, G. W. Huber, M. Boudart, *Principles of Heterogeneous Catalysis*, chapter 1.1, John Wiley & Sons, Ltd **2008**.
[72] G. Bergeret, P. Gallezot, *Particle Size and Dispersion Measurements*, chapter 3.1.2, pages 738–765, John Wiley and Sons, Ltd **2008**.

Manuscript received: February 23, 2024
Revised manuscript received: April 15, 2024
Accepted manuscript online: May 10, 2024
Version of record online: July 22, 2024